Magnetic Resonance in Medicine 67:979–990 (2012)

Understanding Quantitative Pulsed CEST in the Presence of MT

Kimberly L. Desmond[1] and Greg J. Stanisz[1,2]*

Phantom experiments in agar and ammonium chloride were performed to evaluate a three-pool model of magnetization transfer and chemical exchange saturation transfer (CEST) in a pulsed saturation transfer experiment. The utility of the pulsed CEST method was demonstrated by varying the pH of the phantoms and observing the effect upon the CEST spectra both with and without the solid agar (the magnetization transfer pool), while fitting the spectra to the Bloch equation model with exchange. Pulsed CEST could be used to robustly quantify parameters related to CEST, including the exchange rate constant describing proton exchange with free water and the concentration of exchanging protons. Furthermore, the exchange rate constant and the CEST pool offset frequency of the ammonium chloride remained unchanged in the presence of a magnetization transfer pool. The logarithm of the fitted exchange rate constant was linearly related to pH: this relationship was maintained in the presence of magnetization transfer. Magn Reson Med 67:979–990, 2012.

Key words: chemical exchange saturation transfer; magnetization transfer; pulsed CEST

INTRODUCTION

Chemical exchange saturation transfer (CEST) is a magnetic resonance imaging (MRI) technique sensitive to the presence of mobile protons exchanging with water. Chemical exchange was first investigated by nuclear magnetic resonance (NMR) (1–4) and was proposed as an MRI method by Wolff and Balaban (5); however, it was only recently introduced as a clinical technique (6). Its utility as a contrast mechanism has been demonstrated in brain tumors (7,8) and in identification of reperfusable regions of stroke damage (9). As the chemical exchange is sensitive to hydrogen ion concentration, CEST experiments may allow quantification of pH as well. Quantitative measurements of the exchange rate constant and concentration for different lanthanide-based CEST contrast agents have been obtained from phantom experiments (10,11), but in vivo CEST quantification has been less successful. One of the main challenges for producing quantitative CEST measurements in vivo is the added interference of proton exchange with the semi-solid macromolecular protons, the magnetization transfer (MT) effect, that may reduce the asymmetry in the CEST spectra (12).

The CEST experiment generates contrast between voxels containing different proportions of bulk water protons and protons with a different chemical shift. The bulk water protons are those that are freely moving (i.e., with a short correlation time, $\tau_c \sim 10^{-10}$ s) such as those in cytosolic and extracellular water. The off-resonance proton spins, although having a T_2 too short or concentration too low to be detected directly (i.e., through a basic NMR spectroscopy experiment), can be saturated so as to reduce the bulk water signal through exchange of magnetization. This saturation effect is magnified during the radio frequency (RF) irradiation if the exchange rate is faster than the longitudinal relaxation rate of the water, and thus saturation of a small off-resonance pool can have a large effect on the measured water signal. CEST contrast has been defined as resulting from saturation transfer dominated by chemical exchange, as opposed to MT, which evidently occurs mainly as a dipole–dipole interaction (13,14) between water and large macromolecular protons with equivalent Larmor frequency. Complicating matters, a bulk water proton can experience both types of exchange and both have similar observable effect on the net magnetization. As a result, there is much shared theory and terminology between CEST and MT. However, these are several features aside from the exchange mechanism that distinguish the two processes. Chemical balance is affected by pH whereas the dipole–dipole interaction is not, and, in addition, the molecules contributing to CEST are typically free in solution whereas MT arises from water protons bound to immobile macromolecules such as lipids. The MT protons have a short T_2 (~10 μs) resulting in a broad resonance centered at the water frequency, whereas the CEST protons have a longer transverse relaxation time, T_2 (~10 ms) and resonate at a frequency that is offset from water protons due to chemical shift. Therefore, CEST and MT are often treated as separate contributors to saturation transfer. It should be noted, however, that both CEST and MT are measured by the same principal experiment, which is essentially a measurement of the bulk water signal following a RF saturation pulse, and therefore it is not possible to decouple these two effects entirely.

Endogenous to biological tissue, the largest contributors to CEST contrast are amide protons in amino acids (15). Moreover, numerous exogenous contrast agents with suitable frequency shift and exchange properties have been developed that incorporate lanthanides, including paramagnetic CEST compounds (PARACEST) (11) and

[1]Department of Medical Biophysics, University of Toronto, Toronto, Ontario, Canada.
[2]Sunnybrook Health Sciences Centre, Department of Imaging Research, Toronto, Ontario, Canada.
Grant sponsors: The Ontario Institute for Cancer Research, the Canadian Institute for Health Research (Terry Fox Program Project Grant).
*Correspondence to: Greg J. Stanisz, Ph.D., Imaging Research, Sunnybrook Research Institute, 2075 Bayview Avenue, S672, Toronto, Ontario. M4N 3M5. E-mail: stanisz@sri.utoronto.ca
Received 15 October 2010; revised 31 May 2011; accepted 8 June 2011.
DOI 10.1002/mrm.23074
Published online 19 August 2011 in Wiley Online Library (wileyonlinelibrary.com).

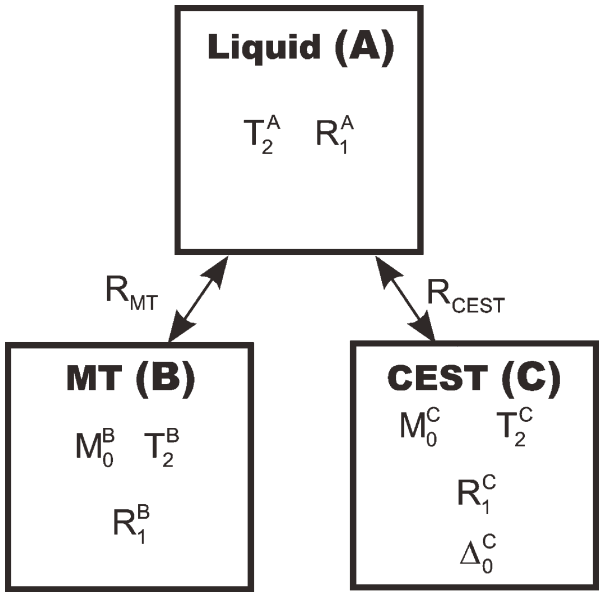

FIG. 1. The three-pool model with exchange. $M_0^{A,B,C}$ are the relative concentration of protons in exchange pools, $T_2^{A,B,C}$ are the transverse relaxation times for each pool, $R_1^{A,B,C}$ the longitudinal relaxation rate, R_{CEST} and R_{MT} the exchange rate constants governing exchange between the water pool with the CEST and MT pools respectively, and Δ_0^C the resonance frequency of the CEST pool (in relation to the liquid pool).

lipoCEST (16). For typical tissues and experimental parameters, the MT effect is present within a wide range of saturation pulse offset frequencies (1–50 kHz), which for scanners of field strength 3T and below encompasses the entire range of endogenous CEST (15), and most of the PARACEST agents currently in development (ranging up to about 500 ppm frequency offset). Thus, for any CEST or PARACEST system under investigation, there is an underlying MT effect which is always present.

This article provides a model of CEST and MT for quantitative determination of CEST characteristics independent of a coexisting MT pool. Data were obtained with a pulsed CEST experiment, by acquiring a series of images with varying offset frequency (saturation spectra) and repeating for several different saturation pulse amplitudes. We present a three-pool model with CEST and MT exchange that was fitted to the experimental data for CEST, MT, and combined CEST/MT phantoms with varied pH. Below, we discuss the theoretical approach and experimental considerations.

THEORY

A three-pool model was used, consisting of a bulk water (liquid pool, "A"), semi-solid (MT pool, "B") and labile pool (CEST pool, "C"), which had been suggested as an extension to two-pool MT theory (17) and investigated by Li (18). It is similar in concept to the three-pool models developed by Tessier (19) for describing multipool MT and Woessner who studied PARACEST agents with multiple labile groups (20). Although some cases necessitate the inclusion of more than one MT pool (19,21–23), we chose here to limit the number of MT pools to one as it is sufficient to describe MT effects in agar (17). The framework of the model used in this article is illustrated in Fig. 1.

The amount of exchange between the CEST and MT pools compared with exchange with water was assumed to be negligible on the basis of their limited concentration with respect to free water, so this interaction was omitted from the model. The Bloch equations describing the behavior of the magnetization in the presence of exchange and RF irradiation are as follows:

$$\begin{aligned}
\frac{dM_x^A}{dt} &= \left(\frac{-1}{T_2^A} - R_{\mathrm{CEST}}M_0^C\right)M_x^A - 2\pi\Delta M_y^A + R_{\mathrm{CEST}}M_0^A M_x^C \\
\frac{dM_y^A}{dt} &= 2\pi\Delta M_x^A + \left(\frac{-1}{T_2^A} - R_{\mathrm{CEST}}M_0^C\right)M_y^A + \omega_1 M_Z^A \\
&\quad + R_{\mathrm{CEST}}M_0^A M_y^C \\
\frac{dM_z^A}{dt} &= -\omega_1 M_y^A + (-R_l^A - R_{MT}M_0^B - R_{\mathrm{CEST}}M_0^C)M_z^A \\
&\quad + R_{MT}M_0^A M_z^B + R_{\mathrm{CEST}}M_0^A M_z^C + R_l^A M_0^A \\
\frac{dM_z^B}{dt} &= R_{MT}M_0^B M_z^A + (-R_l^B - R_{rfb} - R_{MT}M_0^A)M_z^B + R_l^B M_0^B \\
\frac{dM_x^C}{dt} &= R_{\mathrm{CEST}}M_0^C M_x^A + \left(\frac{-1}{T_2^C} - R_{\mathrm{CEST}}M_0^A\right)M_x^C \\
&\quad - (2\pi\Delta - 2\pi\Delta_0^C)M_y^C \\
\frac{dM_y^C}{dt} &= R_{\mathrm{CEST}}M_0^C M_y^A + (2\pi\Delta - 2\pi\Delta_0^C)M_x^C \\
&\quad + \left(\frac{-1}{T_2^C} - R_{\mathrm{CEST}}M_0^A\right)M_y^C + \omega_1 M_z^C \\
\frac{dM_z^C}{dt} &= R_{\mathrm{CEST}}M_0^C M_z^A - \omega_1 M_y^C \\
&\quad + (-R_1^C - R_{\mathrm{CEST}}M_0^A)M_z^C + R_1^C M_0^C
\end{aligned} \tag{1}$$

where $M_{x,y,z}^{A,B,C}$ define the magnetization in each Cartesian coordinate, $M_0^{B,C}$ the equilibrium magnetization relative to equilibrium magnetization in the liquid pool, M_0^A, $T_2^{A,B,C}$ the transverse relaxation times for each pool, $R_1^{A,B,C}$ the longitudinal relaxation rates, ω_1 the amplitude of the RF saturation pulse (in rad/s), Δ_0^C the resonant frequency of the CEST pool and Δ the offset frequency of the RF irradiation (both in Hz, in relation to the liquid pool, A). R_{rfb} represents the RF absorption profile for the MT pool, which differs from the Lorentzian lineshape (arising from exponential signal changes subsequent to RF absorption and single-component T_2 decay) due to cross-relaxation from spin–spin interactions (24). R_{CEST} and R_{MT} are the fundamental exchange rate constants describing the exchange between the water pool and the CEST and MT pools, respectively. In this formulation we followed Henkelman's notation (17), such that R_{CEST} and R_{MT} represent the rate of change of the magnetization in the pools when the individual pools are equal in size. To satisfy the equilibrium condition, the following conditions need to be met: $k_{BA}M_0^B = k_{AB}M_0^A = R_{MT}M_0^A M_0^B$ and $k_{CA}M_0^C = k_{AC}M_0^A = R_{\mathrm{CEST}}M_0^A M_0^C$ where the k terms represent the pseudo first order rate constants describing exchange in the direction specified by the subscripts, i.e., k_{BA} describes exchange from pool B to pool A. Given the equations above, these rates can be formulated in terms of the fundamental exchange constants and the

equilibrium magnetization in each pool. In this work, all magnetizations were normalized by M_0^A. This yields $M_0^A = 1$ and renders the pseudo first order rate constants k_{CA} and k_{BA} equal to R_{CEST} and R_{MT}, respectively.

Only the longitudinal exchange in the MT pool was considered as it was assumed that the net transverse dipole–dipole interaction was negligible due to the fact that the MT pool T_2 is short enough to destroy the transverse signal on a much shorter timescale than the exchange is occurring at (25). The effects of the remaining transverse MT-pool terms were incorporated into the R_{rfb} term (17).

As done previously in quantitative MT experiment to reduce the number of degrees of freedom in the model, the intrinsic longitudinal relation rate of the liquid pool, R_1^A was computed in terms of the other modeled parameters and the liquid pool longitudinal relaxation time observed in a standard experiment in the absence of saturation, T_{1obs} (17). This is possible as T_{1obs} represents the longitudinal recovery, which is observed after the exchanging pools have reached equilibrium and thus is sensitive to their relative sizes. The methods of calculation of R_1^A for the two-pool model and the extension to the three-pool model are presented in Appendix 1.

EXPERIMENTAL METHODS

Three sets of phantoms with properties of CEST, CEST/MT and MT were prepared in 50-mL plastic vials. Each phantom set consisted of five samples with different pH values. Moreover, each phantom set was prepared three times to assess data reproducibility. The MT pool consisted of 2% agar (Sigma-Aldrich, A7002) solution by weight, and a CEST pool was created by adding 1-M ammonium chloride (NH_4Cl, Sigma-Aldrich, A4514). The combined CEST/MT phantoms contained both 2% agar and 1-M ammonium chloride. The pH of each phantom was modified by adding a 10-mM buffer prepared from citric acid and sodium citrate at a pH value ranging from 5 to 6 in increments of 0.25 pH units. A reduction of 0.5 pH units occurred in all phantoms upon mixing the citric acid buffer with the ammonium chloride, and therefore the five samples in each of the phantom sets had pH values ranging from 4.5 to 5.5 in increments of 0.25 pH units.

Agar is structured as an aggregation of helical polysaccharides (26) interspersed with pores whose size is inversely proportional to agar concentration (27). It was chosen as a model for MT processes as it has MT properties similar to tissue in that it contains both a restricted and free water pool, with similar macromolecular content and exchange rate constant for concentrations less than 10% by weight. Agar has been frequently used as an MT model in previous literature (17,28). In addition, agar closely mimics tissue properties in that the dominant mechanism for MT is through whole-molecule exchange of water (14,29). One notable difference is that the RF absorption lineshape of agar is described by a Gaussian function (17) rather than the super-Lorentzian observed in most tissues (30), which determines the form of R_{rfb} used in the modeling.

Ammonium chloride (NH_4Cl) provides a good model for endogenous CEST (5), as it is highly soluble in water (resulting in a uniform CEST effect across the sample) and has four equivalent hydrogen atoms per molecule, resonating at ~2.4 ppm higher frequency than the water resonance, which is in the same range as the ~3.5 ppm observed for endogenous amide protons in tissue. Both ammonium chloride and amide protons have a base-catalyzed proton exchange for pH above 4.5 (31). According to Bronsted's catalysis law (32), the logarithm of the CEST exchange rate constant (R_{CEST}) is expected to vary linearly with the logarithm of the acidity of the solution (pK_a): $R_{CEST} = -\alpha\ pK_a + C$, where C is a constant and α varies between 0 and 1 and represents the motional restriction of the exchanging particle which approaches a slope of 1 in the diffusion-limited case.

If the ammonium chloride and agar exist as independent systems when combined in solution then the CEST exchange rate constant, R_{CEST}, is not expected to change in the presence or absence of the MT pool. For this to be true, it implies that the pore size of the agar must be sufficiently large as not to significantly impede the motion of the ammonium chloride molecules and that no chemical bonds are formed between the ammonium chloride and agar.

MR Experiments

In the ideal saturation transfer application, the amplitude of the saturation pulse is kept constant and is on for the duration of the experiment (the continuous wave, CW, experiment). In this case, the signal reaches a saturation steady state, and the analysis is simplified because it is possible to set all the time derivatives in Eq. 1 to 0 and solve Eq. 1 to provide an algebraic formula for the magnetization in each of the pools as a function of relaxation rates, exchange rate constants and saturation pulse characteristics.

It is currently not practical, however, to deliver CW irradiation on most clinical systems since there is usually only one channel for RF transmission. As a result, in many imaging applications, the duration of the saturation pulse is long enough for the system to reach steady state (>5 times T_1) but is off during the image acquisition. Often, though, there are also restrictions on the maximum RF pulse length, which prevent pulses of sufficient length to reach the steady state within one sequence repetition time (TR) and can result in TRs that are too long to be amenable to in vivo applications. To mimic the clinical setting, we used a compromise consisting of a standard spoiled gradient-echo sequence with the addition of a single shaped saturation pulse once per TR (33). We will refer to this sequence as "pulsed CEST". For example, if the typical pulse is 15 s long to achieve steady state in one TR, the pulsed CEST sequence can achieve an equivalent spectrum (34) by increasing the peak amplitude of the shaped saturation pulse by a factor of 4, reducing the pulse length to 0.1 s and using the minimum TR that accommodates this pulse. Several iterations of the pulsed CEST sequence are required before the spoiled gradient-echo steady state is achieved.

The Bloch equations in the presence of pulsed RF were obtained by replacing the RF amplitude, ω_1, in Eq. 1 with the time varying $\omega_1(t)$. In general, this complicates

Table 1
CEST and MT Sequence Parameters

TR [ms]	Excitation pulse angle [°]	MT pulse duration [ms]	Max B_1 amplitude [μT]	Effective saturation pulse angle [°]	Δ Sampling range (45 points total) [kHz]
200	38	106	0.88	500	−0.8 to 200
			1.75	1000	
			4.38	2500	
			6.92	3835[a]	

[a]The maximum value of the RF saturation pulse angle was restricted by SAR limits.

the search for an analytical solution since Eq. 1 has become a system of first order, linear differential equations with nonconstant coefficients. Although the solution to Eq. 1 with time varying terms theoretically exists, its complicated form and time dependent integrals make it impossible to provide straightforward and easy-to-compute formulas. To overcome this limitation, we used the piecewise-constant RF approximation proposed by Portnoy and Stanisz (35). In our case, the sampling interval was chosen to be the interval between successive elements comprising the shape of the RF pulse.

Although two- and three-pool quantitative modeling of CEST has been proposed previously for the CW experiment, which allows the magnetization to achieve the saturation steady state (18,20,36–38), and using CW approximations for pulse trains (34), we believe this is the first application of the three-pool model to parameter estimation using a pulsed CEST experiment. The model does not require that the signal has reached steady state after one pulse, which allows for a shorter TR and thus a briefer experiment without the introduction of systematic errors in the magnetization calculation caused by using a CW approximation at small offset frequencies (35).

Imaging was carried out on a GE MR750 3T system, using the body coil for RF transmission and the 8-channel phased array head coil (8HRBrain) as a signal receiver. The pulse sequence was based on the vendor's 3D spoiled gradient-echo sequence with MT options enabled. This resulted in the insertion of a saturation pulse at the beginning of every TR. The shape of the saturation pulse was changed from the default Fermi pulse to a Hanning-windowed Gaussian (39), with a cutoff at 3.6 standard deviations from the peak amplitude. Modifications to the sequence code were made to allow control over the offset frequency, duration, and flip angle of the saturation pulse. All sequence parameters chosen for the experiment were within the regulation limits of SAR (2 W/kg) and are listed in Table 1. Each spectrum contained 45 offset frequencies, linearly sampled over the range from −0.8 to 0.8 kHz and then logarithmically sampled from 1 to 200 kHz to capture the features related to both CEST and MT. For each experiment, a 3D volume was acquired consisting of six coronal 5-mm slab encodes with an 18 cm field of view, 64 × 64 matrix size and scan time of 100 s per image. One image was collected for each of the 45 offset frequencies for each of the four RF amplitudes, for a total of 180 images resulting in 5 h imaging time. Data from the first 16 TR periods were discarded to allow the magnetization to reach the spoiled gradient-echo steady state. In addition, four slabs (two from the top and two from the bottom) were discarded due to deviations from the theoretical ideal at the edge of the excitation profile. The voxel-wise signal-to-noise ratio (SNR) was ∼100. Figure 2 shows the arrangement of the phantoms within the scanner, and is representative of the image quality and resolution. Two images are shown, a reference image acquired in the absence of a saturation pulse and an image showing effects of saturation transfer at 300 Hz offset frequency.

Multiple amplitudes of the saturation pulse were required for the experiment to capture the maximum change in signal for a range of CEST and MT parameters and to aid in obtaining a unique solution from the fitting algorithm. Static field, B_0, calibration was performed on-the-fly by adjusting the center frequency so that the minimum signal was achieved at an offset frequency of 0 Hz, which remained valid as long as the experiment was performed in the slow exchange regime ($\Delta_0^C > R_{CEST}$) or the bulk water pool was vastly larger than the CEST pool (as was the case here). This was followed by a fine B_0

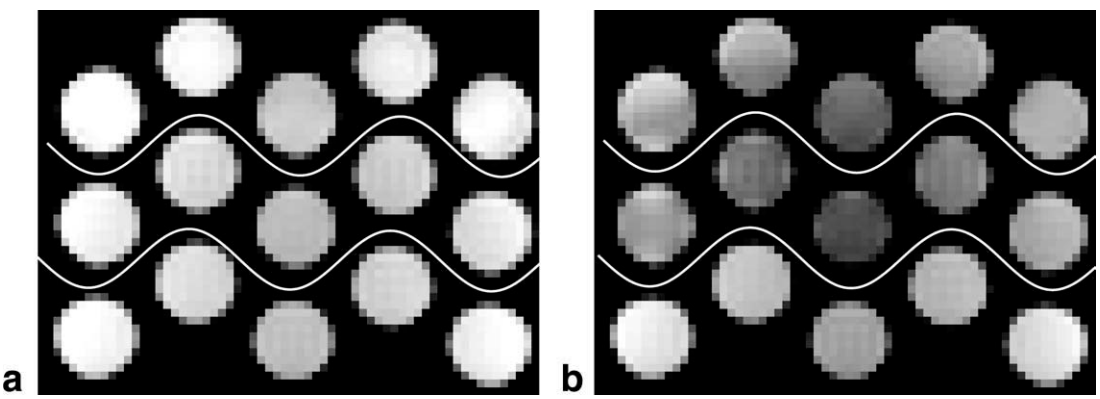

FIG. 2. Phantom arrangement and representative image quality for this study. Images are cropped to 16 cm × 12 cm. Row 1 shows the CEST phantoms, row 2 the CEST/MT phantoms and row 3 the MT phantoms. The range of pH goes from 4.5 on the left to 5.5 on the right of each image. **a**: Image acquired in the absence of a saturation pulse and **b**: 300 Hz saturation pulse frequency offset showing changes in signal due to the CEST effect.

adjustment, which determined the B_0 frequency offset by finding the minimum of a spline fitted to the data (40). B_1 mapping was performed using the spin echo double angle method described in (41), with excitation flip angles of 60 and 120° and refocusing flip angles double those of the excitation angles. The effective T_1 of the phantoms, T_{1obs}, was determined prior to the saturation experiment using a standard inversion recovery experiment with TR of 10 s and inversion times of 500, 1000, 1250, 1750, 2000, 2500, 3000, 3500, and 4000 ms.

Data Analysis

All data analysis was performed in MATLAB (MATLAB 7.3, The MathWorks Inc., Natick, MA, 2006), wherein the Bloch equations were modeled including the effects of the saturation pulse and saturation transfer and fit with MATLAB's *fmincon* function. The saturation pulse shape was specified by a waveform file that contained the relative amplitude of the pulse at 512 points evenly spaced over the extent of the pulse. The pulse length was 106 ms for this experiment, which made the sampling interval equal to 208 μs. Although this approximation was necessary, reducing the sampling interval in simulations resulted in negligible changes to the shape of the modelled spectrum.

There were eight model parameters fit to the experimental data points: R_{MT}, M_0^B, T_2^A, T_2^B, R_{CEST}, M_0^C, T_2^C, and Δ_0^C as defined in the Theory section. $R_{1obs}^A(1/T_{1obs})$ was determined from the independent inversion recovery measurements and used to calculate the model parameter R_1^A as described in Appendix 1. The longitudinal relaxation rate of the MT pool, R_1^B was fixed at 1 s^{-1} as in previous publications (17) as R_1^B is expected to be much slower than either R_{CEST}, R_{rfb} or R_{MT} and thus has little effect on the observed system behavior. For an equivalent reason, the longitudinal relaxation rate of the CEST pool, R_1^C, was also set to 1 s^{-1}. To satisfy the condition that M_0^A equals 1, it was necessary to normalize all the spectra. Reference images were acquired with a saturation pulse frequency offset of 200 kHz at the beginning and end of the acquisition of each spectrum. In this way, if signal drift occurred, it could be retrospectively corrected for by linearly interpolating the change in signal over time.

For each phantom set (CEST, MT or CEST/MT), the data from all pH values was grouped during the fitting by combining the spectra from all five phantoms within the set. This resulted in 20 spectra of 45 frequency offsets each, representing the four saturation pulse amplitudes and five pH values, for a total of 900 data points fit simultaneously in what we refer to as the "global fit." Three global fits were performed, one for each phantom set. In the case of the CEST-only set, MT parameters in Eq. 1 were set to zero. Likewise, for the MT phantoms, CEST parameters were neglected. For each global fit, a single estimate for all parameters was obtained, with the exception of five R_{CEST} parameters (one for each phantom), which were allowed to vary independently with pH. This resulted in a total of 12 free parameters per global fit. At each iteration of the fitting algorithm, 20 model spectra were generated to match the experimental data according to the scanner parameters and the current estimates of the CEST and MT properties for each spectrum. The root-mean-square difference between these model curves and the data was computed, and the parameter set which satisfied the global minimum of this error metric was obtained. Parameter confidence intervals were computed for each global fit according to the method presented in Appendix 2.

After performing the above procedure, there were still some systematic differences between the data and the model, in that the data points from the higher saturation pulse amplitudes appeared shifted from the curve of best-fit. Quantitative MT (and by extension quantitative CEST) methods assume that the independent measurements of B_1 and B_0 inhomogeneities are exact; however, our accuracy was not sufficient for that assumption to be upheld. The structure in the remaining residuals in the fitted model could be described by errors in B_1 and B_0, and therefore, with all other parameters fixed, the fitting was run once more with B_1 and B_0 now allowed to vary. This introduced 10 additional free parameters to the fit; one B_1 and one B_0 corrective factor for each of the five phantoms in the global fit. After this step, the resulting fit was satisfactory (residuals were unstructured and less than 1% of the total signal), and it was not necessary to introduce any additional parameters to the model.

The entire experiment, including sample preparation, imaging, and data fitting was repeated three times to evaluate reproducibility. In reporting the parameter estimates, two major sources of errors were considered: differences between the phantoms due to their preparation and inaccuracies in the fitting procedure due to noise in MR images and the sensitivity of the three-pool model to this noise. During phantom construction, there are inconsistencies in the weighing of the constituents, as well as in the boiling time for the agar. In addition, the noise in the MR images creates residuals in he fitted curves, which create allowances in the parameter estimates which can be expressed as confidence intervals. In particular, we considered how accurately the three-pool model parameters can be determined provided limited SNR, limited experimental range of experimental conditions and possible parameter coupling resulting from the mathematical formalism used (see Appendix 2 for further details). Unless otherwise stated, in the body of the manuscript, we quote the errors in the parameters as standard deviations (SD), which represent the differences between repetitions of the experiment and fitting procedure on the three phantom sets, which captures the errors arising from both sources.

RESULTS

Experiments were conducted according to the protocol in the Methods Section, with data acquired for the three phantom sets having 20 spectra per set including the four saturation pulse amplitudes and five pH values and with 45 offset frequencies in each spectrum. Signal drift was not detectable over the course of the experiments (it was within the image noise), and thus corrections to the images for this factor were not required.

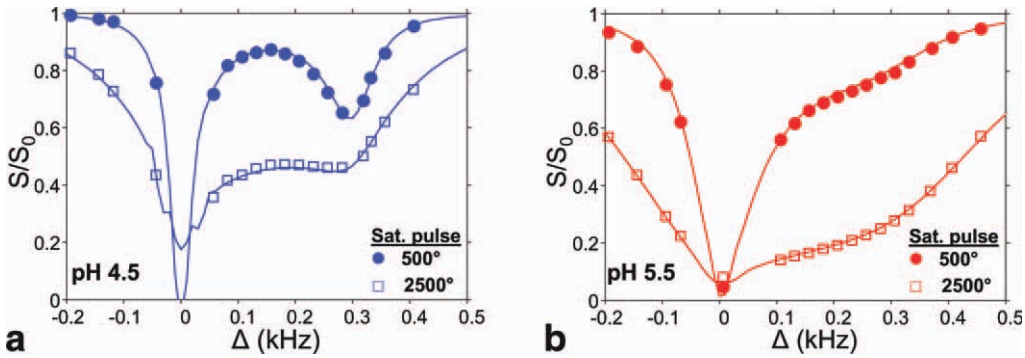

FIG. 3. Fitted spectra from CEST phantoms prepared at (**a**) pH 4.5 and (**b**) pH 5.5. Results are for saturation pulse flip angles of 500° and 2500°. Solid lines represent the fitted model (global fit to all pH). Fits were performed across all collected data points; however, only the range from −0.2 to 0.5 kHz is shown to highlight the changing portion of the spectra.

The longitudinal relaxation rates, T_{1obs}, were estimated from the inversion recovery data. T_{1obs} did not change as a function of pH, and was 3180 ± 120 ms for the CEST phantom sets; 2570 ± 110 ms for CEST/MT sets; and 2530 ± 100 ms for MT sets. The error represents the standard deviations across the three repetitions of the experiment.

A large variation in the appearance of the CEST spectra was observed over the experimental pH range (see Fig. 3). Figure 3 shows the features of the CEST spectra for pH 4.5 (4a) and pH 5.5 (4b) at saturation pulse flip angles of 500° and 2500°. The CEST effect was most pronounced at ~300 Hz (2.35 ppm) for a flip angle of 500° and was greatest at pH 4.5. As the pH increased, the distance between the minima of the direct effect (free water saturation) and the maximum CEST effect decreased. The width of the direct effect increased, and the appearance of the CEST effect became less sharp.

After the B_1 and B_0 correction, there was a very good agreement between the experimental data and the fitted model, with the maximum average residual (over all offset frequencies) not exceeding 1% for any individual spectrum. Figure 4 shows an example of the fit before and after the final B_1 and B_0 correction. This improved the quality of the fit, resulting in the reduced χ^2 value changing from ~20 (which implied a poor fit) to ~1 (implying a good fit which was not overdetermined) and improving the visual clarity of the fitted curves.

Figure 5 shows spectra from the MT-only phantoms at all saturation pulse amplitudes and for pH values of 4.5 and 5.5, covering both ends of the experimental range of pH. The signal attenuation due to the MT effect for 2% agar was less than 15% of the water signal; however, it was most evident in the range above 1000 Hz offset frequency. A much stronger manifestation of the addition of the agar was the change in T_2^A evident in the shifting of the half-maximum of the direct effect to higher and lower frequencies as the observed T_2 decreased. Essentially no changes in the MT spectra were observed with changing pH, as expected for a magnetization exchange dominated by through-space dipole-dipole interactions (14). This also demonstrated that the addition of the ammonium chloride and citric acid at this range of pH did not differentially affect the solidification of the agar.

Representative fitted spectra for pH 4.5 CEST, MT, and CEST/MT phantoms are presented in Fig. 6 to allow comparison of the spectra from the three phantom sets. A logarithmic scale was chosen for the offset frequency

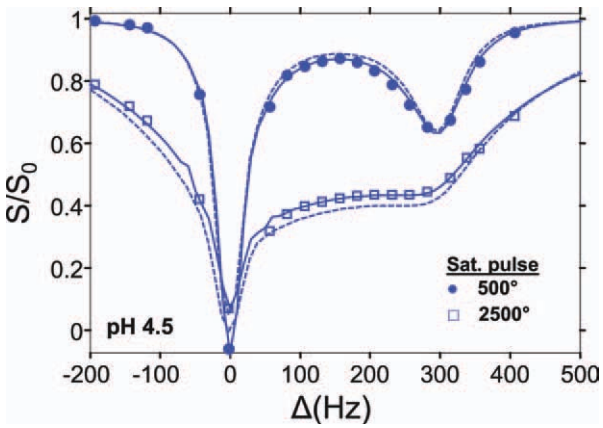

FIG. 4. Comparison between model fitting before and after the B_1 and B_0 correction. Fitted spectra are shown from CEST phantoms prepared at pH 4.5 for saturation pulse flip angles of 500° and 2500°. The dashed line is the original modelled curve, and the solid line shows the results of the fitting after the correction.

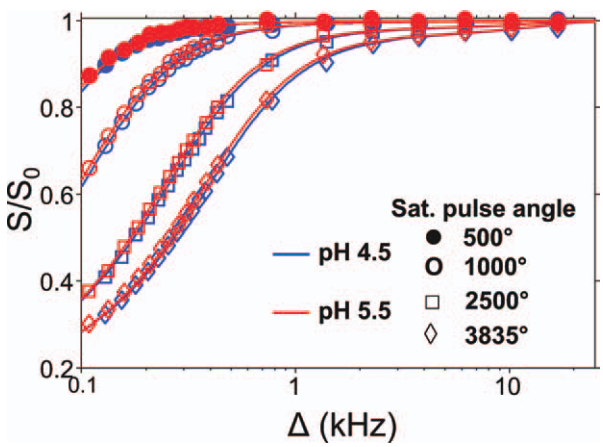

FIG. 5. Normalized signal, S/S_0 as a function of offset frequency, Δ, for a logarithmic set of frequencies from 0.1 to 20 kHz for four different saturation powers in agar MT phantoms.

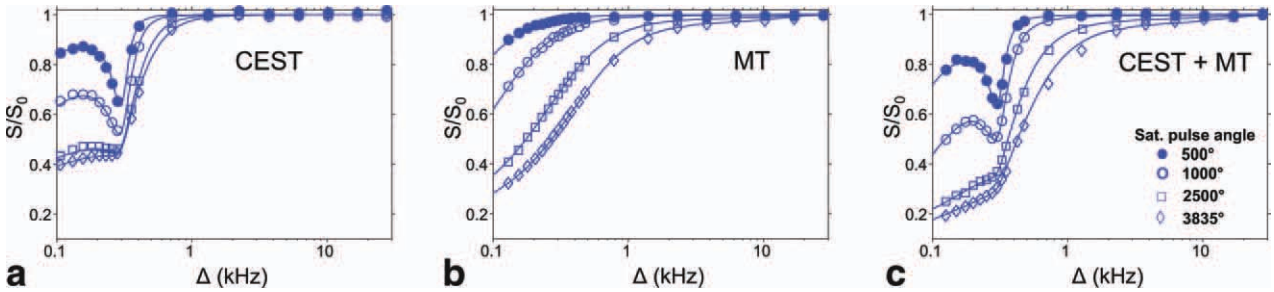

FIG. 6. Fitted CEST spectra for pH 4.5 (**a**) CEST, (**b**) MT and (**c**) CEST/MT phantoms. Normalized signal, S/S_0, is plotted as a function of offset frequency, Δ, for a logarithmic set of frequencies from 0.1 to 20 kHz for four different RF saturation powers. A semi-log axis was chosen so that the MT effects would be visible.

axis so that both the CEST and MT effects could be visualized effectively. Only the data points for the saturation pulse angle of 500° are shown to avoid clutter and to maximize the appearance of the CEST effect. Figure 6 shows the quality of the fit and emphasizes the changes in the spectra that occurred in the presence or absence of the CEST and MT pools. Most importantly, the CEST/MT spectrum was not simply an addition of the CEST and MT spectra, indicating that the effects of each pool on the MR signal were not independent. This confirms experimentally the results of a previous simulation, which predicted that the amplitude of the CEST effect would change if there was also an MT pool present (12).

The results of the global fitting of the data to the three-pool CEST model of the Bloch equations are presented in Fig. 7. Each value in the diagram is the mean and standard deviation of the results from the three repetitions of the experiment. A student's *t*-test revealed that the fitted values for R_{CEST}, Δ_0^C, M_0^B, and T_2^B, which were not expected to change, all did not vary significantly between the phantom sets. The significance level was chosen to be $P = 0.1$, reflecting the small sample size. M_0^C, T_2^A, and T_2^C fit accurately (standard deviation, SD < 7%) in the solid, agar-containing phantoms, however, the model was not sensitive to the transverse relaxation time, T_2^C, in the CEST-only phantoms (SD > 40%). The standard deviation includes both the error introduced in the construction of the phantoms, as well as the error in the parameter estimates as a consequence of noise in the data. For further discussion on the effect of noise on the parameter fitting, please refer Appendix 2.

In Fig. 8, $\log(R_{CEST})$ was plotted versus the global fit pH value for both the CEST and CEST/MT phantom sets and a linear fit was performed. The correlation coefficient for both sets of data was > 0.999.

DISCUSSION

The results of this study illustrate the use of pulsed CEST to obtain quantitative estimates of CEST parameters including the exchange rate constant, concentration, and relaxation properties in a phantom experiment in the presence or absence of agar and ammonium chloride across a range of pH.

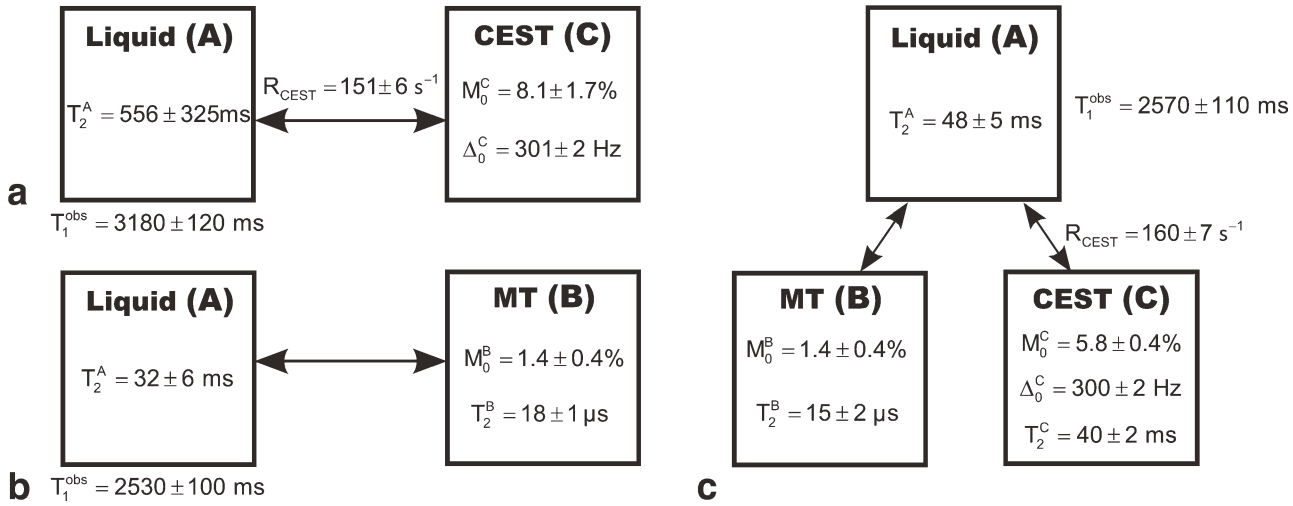

FIG. 7. Compartmental diagrams showing the observed T_1 values and parameters which were successfully fit to the model for each of the three phantom types (**a**) CEST, (**b**) MT, and (**c**) CEST/MT. The CEST exchange rate constant, R_{CEST}, was shown only for pH 4.5. In full, the fitted values for R_{CEST} for the pH range from 4.5 –5.5 for the CEST phantoms were: 151 ± 6, 237 ± 6, 356 ± 17, 556 ± 30, and 939 ± 37 Hz. For the CEST/MT phantom the fitted values for R_{CEST} were 160 ± 7, 246 ± 18, 373 ± 8, 573 ± 22, and 966 ± 32 Hz. Errors shown are the standard deviations between results from the three experiments. R_1^B and R_1^C are not shown because they were fixed to 1 s^{-1} for all analysis.

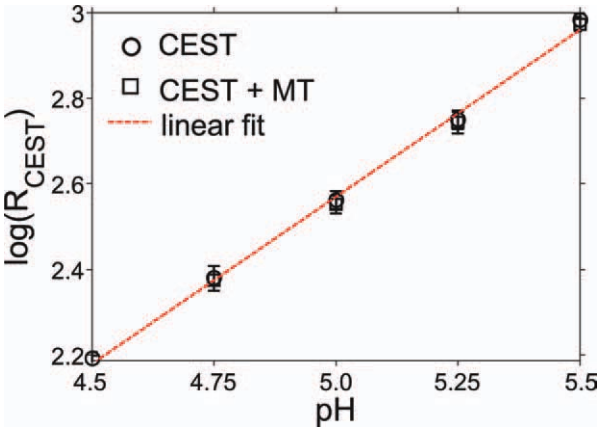

FIG. 8. The linear relationship between $\log(R_{CEST})$ and pH in the range from pH 4.5 to 5.5. $pH = 1.28 \times \log(R_{CEST}) + 1.73$. [Color figure can be viewed in the online issue, which is available at wileyonlinelibrary.com.]

It is apparent from Fig. 3 that the range of pH of ammonium chloride chosen for this experiment represented intermediate exchange. The CEST effect, while well defined at pH 4.5, diminishes as the pH increases and the exchange rate approaches that of coalescence. At pH 5.5, the direct effect and the CEST effect are beginning to merge, and with further increases to pH the ability to uniquely determine the CEST parameters would be lost.

The parameters which were fit with the greatest stability were the CEST exchange rate constant (R_{CEST}) and the frequency offset of the CEST pool (Δ_0^C). The standard deviation of both of these parameters was less than 6% between the three repetitions of the experiment. Furthermore, R_{CEST} and Δ_0^C from the CEST and CEST/MT set global fits were equal to within the parameters' confidence intervals. From these results, it can be concluded that these CEST parameters can be determined independently of an MT pool. In the case of Δ_0^C, which did not vary with pH, it suggests that an a priori measurement of this value could be made and used in future experiments where the CEST pool arises from the same molecular species. It would not be necessary to perform the entire experiment to gain an estimate of Δ_0^C: in separate fits of the pH 4.5 and pH 5.5 CEST/MT data sets from a single experiment, it was possible to obtain $\Delta_0^C = 298$ Hz $\pm$ 2% and 300 Hz +1% −4% respectively (error values are confidence intervals as discussed in Appendix 1). Likewise, the CEST exchange rate constant, R_{CEST}, was determined to be 142 s^{-1} +10% −4% for the from the pH 4.5 data and 958 s^{-1} +15% −3% from the pH 5.5 data.

For the CEST/MT phantom set, the model parameters were similar to those obtained for CEST- and MT-only with the exception of the CEST pool fraction, M_0^C. Interestingly, the errors in M_0^C estimates due to the fitting procedure were small for all phantom sets (confidence interval in the fit for all M_0^C values $< 5\%$); however, there was a difference in the mean M_0^C between the CEST and CEST/MT sets. M_0^C was moderately reduced in the presence of MT, with the mean and standard deviation changing significantly ($P < 0.1$) from 8.1 $\pm$ 1.7% to 5.8 $\pm$ 0.4%. This could be caused by a reduction in the number of available proton exchange sites when the ammonium chloride is encased within the solid agar, but not affecting the CEST exchange rate constant. This decrease is further demonstrated by the smaller CEST effect at 300 Hz for the CEST/MT phantom as seen in Fig. 6.

In the CEST-only phantom data, we observed a coupling between transverse relaxation times of the liquid, T_2^A, and CEST pool, T_2^C, that made it difficult to accurately determine either parameter. Moreover, the value for T_2^A was largely determined by the offset frequency at the half-maximum of the direct effect, which was shifted toward lower frequencies as T_2^A increased and thus was sampled by fewer experimental data points. It was likewise difficult to accurately determine the MT exchange rate constant, R_{MT}, as the minimization function for this parameter was very shallow. This was consistent with the observation made by Portnoy and Stanisz (35) that it is only possible to determine the range of R_{MT} and not necessarily its exact magnitude given the limited set of frequency offsets and using pulsed saturation. Similar to the correlation noted between R_{MT} and the MT pool fraction, M_0^B, in previous studies on agar (17), we obtained a high correlation coefficient for R_{CEST} and M_0^C. The cause of these correlations has a similar root; in several places, these parameters appear multiplied together in the differential Bloch equations (Eq. 1), which makes it difficult for them to be disentangled by the fitting algorithm.

Given that there are four exchange sites per molecule of NH_4Cl, and the CEST phantoms contain 1M NH_4Cl in 55M water, this yields a 7.2% concentration of NH_4Cl protons. This value agrees with the fitted one of 8.1 $\pm$ 1.7% for the concentration of CEST pool protons, M_0^C. The chemical shift of NH_4Cl reported in the literature is 2.4 ppm (480 Hz at 4.7 T (5)), which is consistent with the value of 2.35 ppm obtained in this work ($\sim$300 Hz at 3 T). 2% agar prepared at neutral pH was found to have a concentration of protons in the macromolecular pool, M_0^B, of 0.51 $\pm$ 0.1% and a T_2^B of 12.9 $\pm$ 0.1 μs (17) compared with 1.4 $\pm$ 0.4% and 17.7 $\pm$ 1.1 μs in this work. This mismatch could be attributed to either the large difference in pH between the agar samples in the two studies, or the differences in chemical formulation of the agar between manufacturers.

There were also differences in the observed longitudinal relaxation, T_{1obs}, and the transverse relaxation time for the liquid pool, T_2^A between this study and other published values. In the literature for 2% agar, $1/R_{1obs} = T_{1obs} = \sim$2040 ms (17) and T_2^A was 60 ms while we observed 2550 and 35 ms, respectively. We attribute the changes in T_2^A, T_2^B, and M_0^B to differences in the agar structure between neutral pH and the 4.5–5.5 pH range caused by the addition of the citric acid buffer, which was not an element of the earlier experiments.

Quantitative CEST vs. CEST Asymmetry

In this study, we found a linear relationship between $\log(R_{CEST})$ and pH regardless of the presence of the MT pool (Fig. 8). This is expected if the exchange is entirely in the acid- or base- catalyzed regime such that the proton exchange rate is proportional to the number of protons that are free in solution (31).

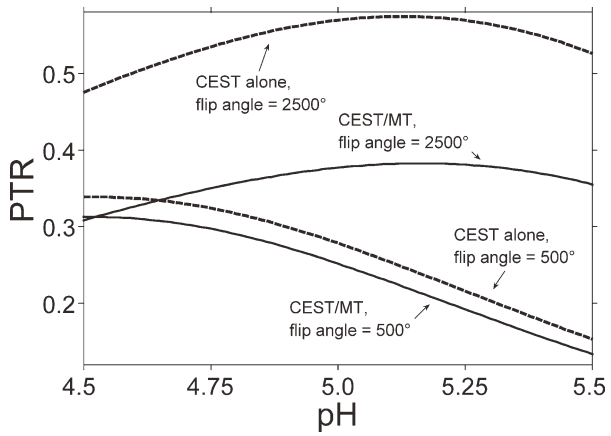

FIG. 9. The theoretical proton transfer ratio (CEST asymmetry) is plotted as a function of pH for both CEST and CEST/MT phantoms types and saturation pulse flip angles of 500° and 2500°. The values for R_{CEST} used in the simulation were determined according to the relationship between pH and R_{CEST} derived in Fig. 8 and the other parameters were taken from the results of the fitting as shown in Fig. 7.

This quantitative method of pH determination was compared with the most commonly used experiment for observing the CEST effect, called the "CEST asymmetry" or "proton transfer ratio" method (6–8,42) proposed by Zhou (6). Three images are typically acquired, one with saturation at the resonance frequency offset of the CEST pool: $S(\Delta_0^C)$, one at the frequency of opposite sign $S(-\Delta_0^C)$, and a reference image without saturation: S_0. This is analogous to the method of creating MT ratio images, but with the symmetric component of MT subtracted. An asymmetry image is created by calculating proton transfer ratio = $[S(-\Delta_0^C)-S(\Delta_0^C)]/S_0$ (38). CEST properties determined from asymmetry measurements require that the CEST effect changes independently of the properties of the MT pool. It is also dependent on the sequence parameters (including RF amplitude and shape), which may cause difficulties in comparing results between different studies.

In Fig. 9, the CEST asymmetry is simulated as a function of pH for both the CEST and CEST/MT phantom types according to the parameter estimates from this study and the relationship between R_{CEST} and pH determined from Fig. 8. The relationship between pH and asymmetry is nonlinear, and changes depending upon the choice of saturation pulse amplitude and the presence of an MT pool. This exemplifies the fact that the asymmetry method may not be robust under situations of changing macromolecule concentration, and a relationship between CEST asymmetry and pH derived without accounting for these factors may be invalid.

Reduction in the MT Contribution

It is possible by referring to Eq. [1] and by choice of experimental parameters to minimize the contribution of the MT pool to the signal and thus preserve the utility of asymmetry analysis. It can be concluded from Fig. 9 that a choice of a lower saturation pulse amplitude (in this case, an effective saturation flip angle of 500°) much reduces the difference between the CEST and CEST/MT results for asymmetry as a function of pH. However, there is a risk that this choice of parameters will not be optimal for maximizing the sensitivity of the experiment to changes due to CEST.

Although this work focused on a CEST pool which is representative of the endogenous labile proton groups, the method is equally applicable to PARACEST and other CEST-based contrast agents with an offset frequency which can be orders of magnitude greater than the endogenous contributors. In this case, another factor that can be chosen to reduce the effects of MT on the CEST measurements is the B_0 field strength. The bandwidth of the MT effect is only dependent on the T_2 of the MT pool, T_2^B, therefore its extent in offset frequency does not change much with increasing field strength. The resonance frequency of the CEST effect, however, is proportional to the field strength. If the B_0 field strength is sufficiently high, the CEST effect could be shifted out beyond 50 kHz where the MT effect is negligible. The CEST protons can then be saturated without affecting the MT pool. Imaging at higher field strength, however, brings its own challenges. For one, the availability of clinical scanners at field strengths higher than 3T is limited, the absorbed RF power increases approximately with the square of the field strength (43) and B_1/B_0 inhomogeneities significantly increase. It is not clear that a gain in CEST contrast would be possible at higher field strengths within the safe limit of human RF absorption.

Using different PARACEST contrast agents could also reduce the impact of the MT effect on the CEST-related signal (18); however, the maximum discovered resonance shift is around 500 ppm, which is still insufficient to completely avoid the MT-affected region of the spectrum for field strengths of 3T and below.

In vivo Application

With the current protocol, one image took 100 s to acquire for a total acquisition time of 5 h for 45 offset frequencies at four saturation pulse amplitudes. Although the total imaging time was substantial, this acquisition involved a dense sampling of the offset frequency range to capture the large variation in behavior between phantoms of differing pH. With some a priori knowledge about the expected range of quantitative CEST and MT parameters, the choice of offset frequencies and saturation pulse amplitudes could be optimized so as to decrease the scan time while improving the sensitivity of the experiment to changes in CEST parameters, similar to what has been accomplished with two-pool models of MT (44,45). As there are eight free parameters in the model, in the absence of noise and correlated parameters only nine points on the spectrum would be required to obtain a unique solution. This would reduce the scan time to under 20 min. More realistically, for the same SNR as obtained in these experiments, we expect to be able to reduce the number of acquisitions to ~20 (10 offsets each for two saturation pulse amplitudes). In cases where the anatomy of interest is localized, a 2D scan could be implemented instead of the 3D scan used in these experiments, which would further reduce scan

time by approximately a factor of six. Paired with a fast acquisition method, such as echo-planar or parallel imaging, it is reasonable that the quantitative pulsed CEST experiment could be performed in a time amenable to in vivo application.

In vivo, for either the case of endogenous CEST or PARACEST, the concentration of the exchanging protons is considerably smaller (on the order of 1–100 mM; 72 mM for amide protons (6)), and therefore the relative influence of the MT pool is enhanced over the phantoms used in this article. The MT pool size fraction, M_0^B, is also typically in the range of 5–20% (46), which is larger than the 1.4% reported for the agar in this article. These two factors increase the contribution of MT to the in vivo saturation transfer experiment and further affect the asymmetry measurements (12), highlighting the need for an MT-independent measure of CEST.

CONCLUSIONS

The pulsed CEST method has been shown to provide consistent results for calculating CEST-related parameters in the presence of a MT pool in a phantom study. This will assist in the determination of pH and exchangeable proton concentration from in vivo CEST experiments using PARACEST contrast agents or measuring the properties of endogenous CEST contributors such as those of amide proton transfer.

ACKNOWLEDGMENTS

K.L.D. acknowledges an Ontario Graduate Scholarship in Science and Technology.

APPENDIX A

Computation of R_1^A for Two- and Three-Pool Models

We first considered the behavior of the longitudinal component of the magnetization in the two-pool system in the absence of RF irradiation:

$$\begin{aligned}\frac{dM_z^A}{dt} &= (-R_1^A - R_{MT}M_0^B)M_z^A + R_{MT}M_z^B + R_1^A M_0^A \\ \frac{dM_z^B}{dt} &= R_{MT}M_z^A + (-R_1^B - R_{MT})M_z^B + R_1^B M_0^B\end{aligned} \quad [A1]$$

The longitudinal relaxation which would be obtained by an inversion recovery experiment is determined by solving this system of differential equations for M_z^A and observing the rate of decay of the exponentials in the solution. As this is a first order system of equations with constant coefficients, the solution has the form:

$$M_z^A = \sum_{i=1}^{2} C_i e^{-\lambda_i t} + M_0^A \quad [A2]$$

where C_i are constants and λ are the eigenvalues of the matrix formed by the coefficients above, and describes the return of the system to equilibrium after the system has been disturbed by the inversion pulse. At some time after the inversion pulse (*TI*), the term with the eigenvalue of smallest magnitude will dominate the behavior of M_z^A; therefore it represents the rate observed in the standard experiment ($R_{1\text{obs}}^A$). Equating this eigenvalue with $R_{1\text{obs}}^A$ yields an expression for $R_{1\text{obs}}^A$ in terms of the other exchange and relaxation rates, including R_1^A. One can isolate R_1^A from this expression, resulting in the following solution (17):

$$R_1^A = R_{1\text{obs}}^A - \frac{R_{MT}M_0^B(R_1^B - R_{1\text{obs}}^A)}{R_1^B - R_{1\text{obs}}^A + R_{MT}} \quad [A3]$$

Likewise, the relationship between the observed T1 and the intrinsic T1 ($1/R_1^A$) of the bulk water in the presence of a CEST pool can be derived from the three-pool exchange-modified Bloch equations in the absence of RF irradiation:

$$\begin{aligned}\frac{dM_z^A}{dt} &= (-R_1^A - R_{MT}M_0^B - R_{\text{CEST}}M_0^C)M_z^A + R_{MT}M_Z^B \\ &\quad + R_{\text{CEST}}M_z^C + R_1^A M_0^A \\ \frac{dM_z^B}{dt} &= R_{MT}M_z^A + (-R_1^B - R_{MT})M_z^B + R_1^B M_0^B \\ \frac{dM_z^C}{dt} &= R_{\text{CEST}}M_0^C M_z^A + (-R_1^C - R_{\text{CEST}})M_z^C + R_1^C M_0^C\end{aligned} \quad [A4]$$

and following the same procedure to obtain the smallest eigenvalue and solve the expression for R_1^A in terms of $R_{1\text{obs}}^A$, thus eliminating it from the set of free parameters. Although a symbolic expression for R_1^A was obtained in MATLAB, it was in an unsimplified form and of too great a length to present here.

APPENDIX B

Statistical Errors and Parameter Correlations

This section addresses the errors and correlations that arose in the estimated parameters as a result of the fitting procedure and noise in the data, as well as the choice of sequence parameters.

Parameter correlations were calculated by a modified version of the MATLAB function *nlparci* from the residuals and Jacobian matrix returned by the fitting algorithm (47). The confidence intervals were calculated separately for the grouped data sets from each experiment. After the fit was completed, the χ^2 value was calculated as a function of simulated changes in pairs of model parameters, keeping all other parameters equal. Contour plots of χ^2 levels vs. parameter changes were produced. The confidence intervals were defined as the 2D region of the contour plot within which the χ^2 value does not exceed a target maximum value determined by the following function (48):

$$\chi^2 = \chi_0^2\left(1 + \frac{np}{N - np}F(np, N - np, P)\right) \quad [B1]$$

where χ_0^2 is the original χ^2 of the best-fit curve; N is the number of data points; np, the number of fitted parameters; *P*, the desired confidence level (we have chosen 0.68) and F, the F-distribution function (48). Ultimately, a conservative estimate of the confidence interval was chosen as the maximum and minimum values each parameter could achieve (amongst all two-parameter combinations) without exceeding the target χ^2 value.

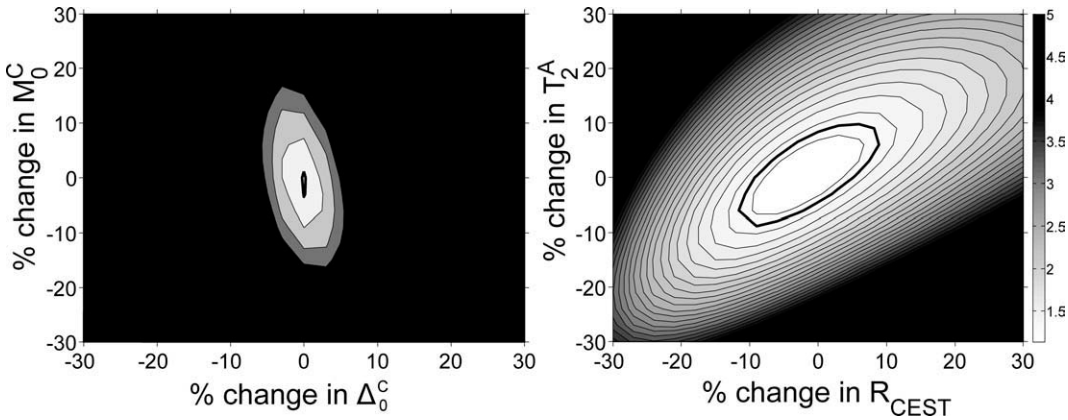

FIG. 10. Contour plot illustrating χ^2 as a function of two parameter pairs: **a**: Changes in the relative size of the CEST pool, M_0^C, and the offset frequency of the CEST pool, Δ_0^C, **b**: Changes in the T_2 of the free water pool, T_2^A, and a linear scale of the CEST exchange rate constant, R_{CEST}. The 68% confidence interval is marked with a heavy outline. There is little correlation between M_0^C and Δ_0^C in a) and thus the accuracy of determining these parameters is high. Figure 10 b), in contrast, shows the strong correlation between T_2^A and R_{CEST}.

Examples of the statistical error analysis of the fitting procedure are shown as contour plots in Fig. 10. The contour color levels in the plots represent the χ^2 value, with a thick outline marking the 68% confidence region calculated from Eq. A2-1. Typically, a large χ^2 value ($>$ 1) is obtained when the model does not accurately fit the data, and a very small χ^2 value ($<$ 1) is obtained when the model is overfitting the data (i.e., if there are more parameters than required for the model to fit the data). Two features of the plots were considered, the width of the 68% confidence region in both dimensions, and whether the region is angled with respect to the axes. A large width occurs when the changes in the shape of the model curve are minimal with respect to changes in the fitted parameter, which is a warning that the parameter is very sensitive to noise in the data. The angled contour occurs when the two parameters are correlated, and thus there is not a unique set of parameters which contribute to the same χ^2 value. Figure 10a shows the response of the χ^2 function to changes in M_0^C and Δ_0^C, as an example of two parameters, which were fit reliably and were uncorrelated. This behavior was typical of most of the combinations of parameters. The response of the χ^2 function for T_2^A and a linear scale of all R_{CEST} values is shown in Fig. 10 b. Correlation between these two parameters is evident as a slope in the contours. The following parameter pairs were also found to exhibit this relationship: R_{MT} and M_0^B, R_{CEST} and M_0^C, and T_2^A, and T_2^C. Despite the existence of some correlation, the confidence intervals for the CEST parameters as determined from the global fits were calculated as follows: M_0^C+1% −4% (unequal upper and lower bounds), R_{CEST} ± 6%, Δ_0^C ± <1%.

REFERENCES

1. Edzes HT, Samulski ET. Cross relaxation and spin diffusion in the proton NMR of hydrated collagen. Nature 1977;265:521–523.
2. Forsén S, Hoffman RA. Study of moderately rapid chemical exchange reactions by means of nuclear magnetic double resonance. J Chem Phys 1963;39:2892–2901.
3. Kalk A, Berendsen HJC. Proton magnetic relaxation and spin diffusion in proteins. J Magn Reson 1976;24:343–366.
4. Stoesz JD, Redfield AG. Cross relaxation and spin diffusion effects on the proton NMR of biopolymers in H2O. Solvent saturation and chemical exchange in superoxide dismutase. FEBS Lett 1978;91:320.
5. Wolff SD, Balaban RS. NMR imaging of labile proton exchange. J Magn Reson 1990;86:164–169.
6. Zhou J, Payen JF, Wilson DA, Traystman RJ, van Zijl PC. Using the amide proton signals of intracellular proteins and peptides to detect pH effects in MRI. Nat Med 2003;9:1085–1090.
7. Jones CK, Schlosser MJ, van Zijl PC, Pomper MG, Golay X, Zhou J. Amide proton transfer imaging of human brain tumors at 3T. Magn Reson Med 2006;56:585–592.
8. Salhotra A, Lal B, Laterra J, Sun PZ, van Zijl PCM, Zhou J. Amide proton transfer imaging of 9L gliosarcoma and human glioblastoma xenografts. NMR Biomed 2008;21(5).
9. Sun PZ, Zhou J, Sun W, Huang J, van Zijl PC. Detection of the ischemic penumbra using pH-weighted MRI. J Cereb Blood Flow Metab 2007;27:1129–1136.
10. Aime S, Delli Castelli D, Fedeli F, Terreno E. A paramagnetic MRI-CEST agent responsive to lactate concentration. J Am Chem Soc 2002;124:9364–9365.
11. Woods M, Woessner DE, Sherry AD. Paramagnetic lanthanide complexes as PARACEST agents for medical imaging. Chem Soc Rev 2006;35:500–511.
12. Desmond KL, Stanisz GJ. Chemical exchange saturation transfer in the presence of magnetization transfer. In Proceedings of the 16th Annual Meeting of ISMRM, Toronto, Canada, 2008:1439.
13. Eng J, Ceckler TL, Balaban RS. Quantitative 1H magnetization transfer imaging in vivo. Magn Reson Med 1991;17:304–314.
14. Swanson SD. Molecular mechanisms of magnetization transfer. In Proceedings of the 18th Annual Meeting of the ISMRM, Stockholm, Sweden 2010.
15. Ward KM, Aletras AH, Balaban RS. A new class of contrast agents for MRI based on proton chemical exchange dependent saturation transfer (CEST). J Magn Reson 2000;143:79–87.
16. Aime S, Carrera C, Delli Castelli D, Geninatti Crich S, Terreno E. Tunable imaging of cells labeled with MRI-PARACEST agents. Angew Chem Int Ed Engl 2005;44:1813–1815.
17. Henkelman RM, Huang X, Xiang QS, Stanisz GJ, Swanson SD, Bronskill MJ. Quantitative interpretation of magnetization transfer. Magn Reson Med 1993;29:759–766.
18. Li AX, Hudson RH, Barrett JW, Jones CK, Pasternak SH, Bartha R. Four-pool modeling of proton exchange processes in biological systems in the presence of MRI-paramagnetic chemical exchange saturation transfer (PARACEST) agents. Magn Reson Med 2008;60: 1197–1206.
19. Tessier JJ, Dillon N, Carpenter TA, Hall LD. Interpretation of magnetization transfer and proton cross-relaxation spectra of biological tissues. J Magn Reson B 1995;107:138–144.
20. Woessner DE, Zhang S, Merritt ME, Sherry AD. Numerical solution of the Bloch equations provides insights into the optimum design of PARACEST agents for MRI. Magn Reson Med 2005;53:790–799.

21. Brooks D, Kuwata K, Schleich T. Determination of proton magnetization transfer rate constants in heterogeneous biological systems. Magn Reson Med 1994;31:331–336.
22. Ceckler T, Maneval J, Melkowits B. Modeling magnetization transfer using a three-pool model and physically meaningful constraints on the fitting parameters. J Magn Reson 2001;151:9–27.
23. Levesque IR, Pike GB. Characterizing healthy and diseased white matter using quantitative magnetization transfer and multicomponent T2 relaxometry: A unified view via a four pool model. Magn Reson Med 2009;62:1487–1496.
24. Swanson SD. Transient and steady-state effects of indirect RF saturation in heterogeneous systems. In Proceedings of the 11th Annual Meeting of ISMRM, Toronto, Canada 1992:255.
25. Solomon I. Relaxation processes in a system of two spins. Phys Rev 1955;99:559–565.
26. Lahaye M, Rochas C. Chemical structure and physico-chemical properties of agar. Hydrobiologia 1991;221:137–148.
27. Pluen A, Netti PA, Jain RK, Berk DA. Diffusion of macromolecules in agarose gels: comparison of linear and globular configurations. Biophys J 1999;77:542–552.
28. Dixon WT, Engels H, Castillo M, Sardashti M. Incidental magnetization transfer contrast in standard multislice imaging. Magn Reson Imaging 1990;8:417–422.
29. Bryant RG. The dynamics of water-protein interactions. Ann Rev Biophys Biomol Struct 1996;25:29–53.
30. Morrison C, Mark Henkelman R. A model for magnetization transfer in tissues. Magn Reson Med 1995;33:475–482.
31. Englander SW, Downer NW, Teitelbaum H. Hydrogen exchange. Annu Rev Biochem 1972;41:903–924.
32. Bronsted JN. Acid and basic catalysis. Chem Rev 1928;5:231–338.
33. Sled JG, Pike GB. Quantitative imaging of magnetization transfer exchange and relaxation properties in vivo using MRI. Magn Reson Med 2001;46:923–931.
34. Sun PZ, Benner T, Kumar A, Sorensen AG. Investigation of optimizing and translating pH sensitive pulsed chemical exchange saturation transfer (CEST) imaging to a 3T clinical scanner. Magn Reson Med 2008;60:834–841.
35. Portnoy S, Stanisz GJ. Modeling pulsed magnetization transfer. Magn Reson Med 2007;58:144–155.
36. Sun PZ, van Zijl PC, Zhou J. Optimization of the irradiation power in chemical exchange dependent saturation transfer experiments. J Magn Reson 2005;175:193–200.
37. Zhou D, Bryant RG. Magnetization transfer, cross-relaxation, and chemical exchange in rotationally immobilized protein gels. Magn Reson Med 1994;32:725–732.
38. Zhou J, Wilson DA, Sun PZ, Klaus JA, Van Zijl PC. Quantitative description of proton exchange processes between water and endogenous and exogenous agents for WEX, CEST, and APT experiments. Magn Reson Med 2004;51:945–952.
39. Sled JG, Pike GB. Quantitative interpretation of magnetization transfer in spoiled gradient echo MRI sequences. J Magn Reson 2000;145:24–36.
40. Stancanello J, Terreno E, Castelli DD, Cabella C, Uggeri F, Aime S. Development and validation of a smoothing splines based correction method for improving the analysis of CEST MR images. Contrast Media Mol Imaging 2008;3:136–149.
41. Insko EK, L. Bolinger. Mapping of the radiofrequency field. J Magn Reson Series A 1993;103:82–85.
42. Jokivarsi KT, Grohn HI, Grohn OH, Kauppinen RA. Proton transfer ratio, lactate, and intracellular pH in acute cerebral ischemia. Magn Reson Med 2007;57:647–653.
43. Uematsu H, Takahashi M, Dougherty L, Hatabu H. High field body MR imaging: preliminary experiences. Clin Imaging 2004;28:159–162.
44. Cercignani M, Alexander DC. Optimal acquisition schemes for in vivo quantitative magnetization transfer MRI. Magn Reson Med 2006;56:803–810.
45. Levesque IR, Sled JG, Narayanan S, Giacomini PS, Ribeiro LT, Arnold DL, Pike GB. Reproducibility of quantitative magnetization-transfer imaging parameters from repeated measurements. Magn Reson Med 2010;64:391–400.
46. Stanisz GJ, Odrobina EE, Pun J, Escaravage M, Graham SJ, Bronskill MJ, Henkelman RM. T1, T2 relaxation and magnetization transfer in tissue at 3T. Magn Reson Med 2005;54:507–512.
47. Seber GAF, Wild CJ. Nonlinear regression. New York: Wiley; 1989. p 775.
48. Draper NR, Smith H, Pownell E. Applied regression analysis. New York: Wiley; 1966. p 407.